Ultrafast Science
A SCIENCE PARTNER JOURNAL

RESEARCH ARTICLE

Gamma-ray Vortex Burst in Nonlinear Thomson Scattering with Refocusing Spiral Plasma Mirror

Weijun Zhou[1,2], Wenchao Yan[1,2]*, Jinguang Wang[3], and Liming Chen[1,2]*

[1]Key Laboratory for Laser Plasmas, School of Physics and Astronomy, Shanghai Jiao Tong University, Shanghai 200240, China. [2]Collaborative Innovation Center of IFSA, Shanghai Jiao Tong University, Shanghai 200240, China. [3]Institute of Physics, Chinese Academy of Sciences, Beijing 100190, China.

*Address correspondence to: wenchaoyan@sjtu.edu.cn (W.Y.); lmchen@sjtu.edu.cn (L.C.)

Citation: Zhou W, Yan W, Wang J, Chen L. Gamma-ray Vortex Burst in Nonlinear Thomson Scattering with Refocusing Spiral Plasma Mirror. *Ultrafast Sci.* 2023;3:Article 0005. https://doi.org/10.34133/ultrafastscience.0005

Submitted 19 September 2022
Accepted 17 November 2022
Published 10 January 2023

The gamma-ray vortex burst in the nonlinear Thomson scattering when the laser wakefield accelerated electron bunch collides with an ultra-intense Laguerre–Gaussian laser that was reflected from the refocusing spiral plasma mirror. The orbit angular momentum of the scattering laser would be transferred to the gamma radiation through the scattering process. The 3-dimensional particle-in-cell simulations gave the electron dynamics in the scattering, which determines the characteristics of the vortical radiation. The radiation calculation results illustrated the burst of gamma-ray vortex and surprisingly revealed the radiation pattern distortion phenomenon due to the nonlinear effect. This scheme can not only simplify the experimental setup for the generation of twisted radiation but also boost the yield of vortical gamma photons. The peak brightness of the gamma-ray vortex was estimated to be 1×10^{22} photons/s/mm^2/mrad^2/0.1% BW at 1 MeV, which might pave the way for the researches on angular momentum-related nuclear physics.

Introduction

The era of vortex beams originally began with the vortex solution for the Maxwell–Bloch equations that was discovered by Coullet *et al.* in 1989 [1]. Three years later, Allen *et al.* [2] demonstrated that the special Laguerre–Gaussian (LG) mode lasers carry the orbit angular momentum (OAM). Since then, the generation and applications of vortex beams have been explored extensively. At present, the vortex beams in the wavelength range from visible to extreme ultraviolet (XUV) have been applied in various fields, including matter manipulation [3], imaging [4], nonlinear optics [5], and quantum optics [6,7]. The vortex beams in this wavelength range could be generated by the common optical devices, such as a spatial light modulator [8], spiral phase plate [9,10], q-plate [11], holograms [12], and high-order harmonics [13,14]. However, the development of the vortex beams in the shorter wavelength range has been limited by technology and conversion efficiency for years [15]. With the development of microfabrication [16] and laser technologies, the generation of vortex beams from the XUV to the soft x-ray range gradually becomes achievable, which could be applied in some important fields, i.e., fundamental physics [15,17,18], microscopy [19,20], spectroscopy [21,22], astrophysics [23–25], and other potential novel applications [26,27]. However, the generation of gamma-ray vortex and the corresponding diagnosis technology remain challenging.

There has been some works that investigated the twisted radiation generation through the Thomson/Compton scattering when the accelerated electron bunch interact with the external vortical electromagnetic field [28–32]. For example, Petrillo *et al.* [33] claimed the generation of kilo-electron volt vortical x-ray when the linac electron bunch at 25 MeV collides with the picosecond LG laser. Moreover, it is proposed to add the helical magnetic undulator in the x-ray free electron laser device to generate the vortical x-ray laser [34,35].

Most of these schemes are based on traditional electron accelerator and the helical 'trigger' field, i.e., the additional vortex laser beam or the helical magnetic field, which would bring unpredictable difficulty and complexity for operations. In addition, laser wakefield acceleration (LWFA) that was driven by the ultrashort high-power laser [36] could accelerate the electron bunch with an ultrahigh peak current and an extremely short bunch duration, which means a much higher peak brightness and time resolution of the radiation than that from the common light sources. For the sake of simplifying the experiment configuration and boosting the yield of vortical high-energy photons, we put forward this configuration that combines the electron acceleration and the vortical radiation generation into one shot using a refocusing spiral plasma mirror (SPM).

In this work, we demonstrated the gamma-ray vortex burst in the nonlinear Thomson backscattering when the accelerated electron bunch from the LWFA collide with the ultra-intense LG laser. A special refocusing SPM was used to refocus the incoming Gaussian laser and simultaneously convert it into the LG mode. The electron bunch from the LWFA has an intrinsic ultrashort duration and a relatively high peak current, which give an ultrafast time resolution and an extremely high peak flux density to the vortical gamma radiation.

Methods

The vortical scattering laser is essential to generate the twisted radiation through the Thomson scattering. As we know, the vector potential of the LG laser could be written as,

$$\vec{a}(\rho,\phi,x,t) = u_p^{|l|}(\rho,x)e^{i\Theta_{klp}(\rho,\phi,x)}e^{-i\omega t}\hat{y}, \quad (1)$$

where the amplitude term,

$$u_p^{|l|}(\rho,x) = a_0 \frac{C_{|l|p}}{\left(1+x^2/x_R^2\right)^{1/2}} \left(\frac{\sqrt{2}\rho}{w(x)}\right)^{|l|} L_p^{|l|}\left(\frac{2\rho^2}{w^2(x)}\right) e^{-\frac{\rho^2}{w^2(x)}}, \tag{2}$$

and the phase term

$$\Theta_{klp}(\rho,\phi,x) = kx + l\phi - \left(2p+|l|+1\right)\tan^{-1}\frac{x}{x_R} + \frac{k\rho^2 x}{2\left(x^2+x_R^2\right)}, \tag{3}$$

in which the $w(x)$, a_0, $L_p^{|l|}$, l, p, and x_R are the waist radius, normalized laser vector potential amplitude, generalized Laguerre polynomials, topology charge, radial index, and Rayleigh length, respectively.

When the electron bunch enters this LG laser field, the dynamics of a single electron would be dominated by the local scattering laser field, as $\vec{\beta}_\perp = \vec{a}/\gamma$. In addition, the radiation field of individual moving charged particle could be calculated by the Liénard Wiechert potential, which determines the distribution of retarded radiation field strength [37],

$$\mathbf{E}_{\mathrm{rad}}(\mathbf{r},t) = \left[\frac{e}{c}\frac{\hat{\mathbf{n}}\times\left(\hat{\mathbf{n}}-\boldsymbol{\beta}\right)\times\dot{\boldsymbol{\beta}}}{\left(1-\boldsymbol{\beta}\cdot\hat{\mathbf{n}}\right)^3 R}\right]_{\mathrm{ret}}, \tag{4}$$

where the $\hat{\mathbf{n}}$, R, $\boldsymbol{\beta}$, and $\dot{\boldsymbol{\beta}}$ present the observation direction, observation distance, normalized velocity, and acceleration of the charged particle, respectively. When the $\boldsymbol{\beta}\cdot\hat{\mathbf{n}}$ term approximate 1, the radiation field strength would reach its peak, which determines the direction of radiation peak. Moreover, the $\dot{\boldsymbol{\beta}}$ term stands for the acceleration of the electron in a laser field, which determines the amplitude and sign of the radiation field strength $\mathbf{E}_{\mathrm{rad}}(\mathbf{r},t)$. This time derivative term would oscillate in the phase that delay $\pi/2$ with respect to the phase of the scattering laser, which could be regarded as the radiation phase of electron. For a real electron bunch, the collective radiation field would be the coherent or incoherent superposition of the radiation generated by individual charged particles. When the electron bunch interact with the vortex laser, the electrons that experience the azimuthal spiral laser phase would also radiate in this spiral phase, which leads to the OAM transfer from the vortex laser to the radiation.

The diagram of our scheme is as shown in Fig. 1, which consists of the electron acceleration stage (Fig. 1A) and the scattering stage (Fig. 1B). The first electron acceleration stage was driven by a normal Gaussian laser in the underdense plasma, which could accelerate the injected electrons to moderate energy. When the driving laser leaves the underdense plasma region, a refocusing SPM at the end would refocus and convert the incoming Gaussian laser into a tightly focused ultra-intense LG laser. Then, the accelerated relativistic electron bunch would head-on collide with the reflected counterpropagating LG laser. The energetic electrons that work as the relativistic Doppler reflectors could absorb abundant fundamental photons and emit a high-energy photon. More importantly, the emitted high-energy photons would simultaneously carry the OAM that was obtained from the scattering LG laser.

Converting the Gaussian driving laser into a tightly focused LG laser is the first key issue in this work. Under the irradiation of the relativistic laser, the normal optical devices would be out of action because of the optical damage for certain, except the plasma mirror. Along with this idea, we put forward the refocusing SPM, which combines the normal spiral phase plate and refocusing plasma mirror. When the intense Gaussian laser impinges on the refocusing SPM, it would be triggered immediately. The reflected laser would compulsively carry the phase term $e^{il\phi}$ by the spiral stair structure and turn into the LG mode as presented in Eq. 1. In the meantime, the incident laser could be tightly refocused into a small spot, and the amplitude of the refocused laser would be amplified dramatically. By choosing an appropriate focus of the refocusing SPM, the peak of the counterpropagating refocused laser could exactly meet the electron bunch at the focal region. Owing to the high intensity of the refocused scattering laser, the interaction would be dominated by the nonlinear Thomson scattering, which would significantly boost the yield of gamma photon [38,39].

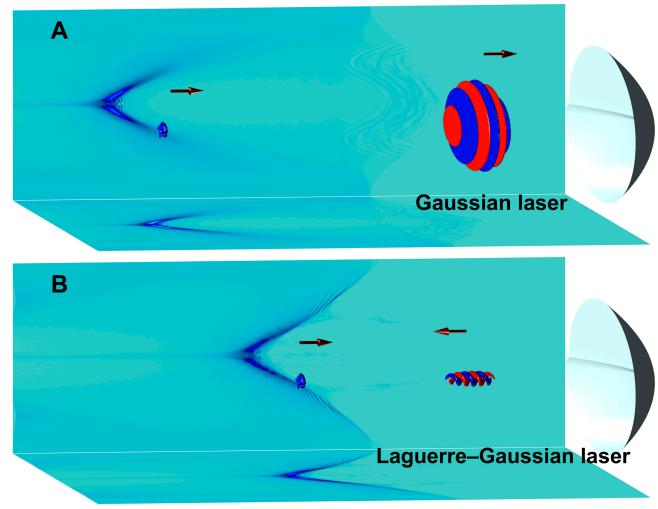

Fig. 1. Diagram of the radiation vortex burst in the nonlinear Thomson scattering with the refocusing spiral plasma mirror (SPM). The subgraphs present the snapshots before (A) and after (B) the laser was reflected by the refocusing SPM, respectively.

Although the spiral phase plate could effectively convert the incident Gaussian laser to the vortex beam, the quality of generated LG laser would be limited by the monochromaticity and wave front of the initial laser beam. When the incident Gaussian laser has a certain bandwidth, the converted vortex beam would be the superposition of different LG modes, in which the designed LG mode is dominant. Therefore, the field distribution of the converted vortex laser would be slightly deformed. In our scheme, the Gaussian driving laser would travel in the underdense plasma for a certain distance at the first stage; the laser wavelength would consequently shift and broaden in this process [40]. As a result, the deformation of the converted LG laser would be inevitable. To minimize the wavelength shift of the driving laser, the shorter laser wavelength, the lower plasma density and acceleration distance were taken in the electron acceleration stage.

Results and Discussion

The full 3-dimensional particle-in-cell (PIC) simulations were performed by the EPOCH code [41]. The size of the simulation box is 30 μm (x) × 40 μm (y) × 40 μm (z), which is divided into 1800 (x) × 320 (y) × 320 (z) cells. In addition, the moving

window was used in the electron acceleration stage. A linearly polarized (y) Gaussian laser launches from the left boundary to the right, and the laser wavelength $\lambda_0 = 800$ nm. The laser temporal profile is also Gaussian, and the pulse duration $\tau = 10T_L$, where the T_L is the laser period. The Gaussian laser focus on the $x = 0.2x_R$ plane with the focal waist radius $\omega_0 = 14$ μm, where the x_R is the Rayleigh length. The focused laser peak intensity is 1.0×10^{19} W/cm^2, which corresponds to the normalized laser vector potential amplitude $a_0 = \frac{eE_y}{m\omega c} = 2.2$. The underdense plasma is composed of the fully ionized helium ions and electrons. The density profile consists of a $0.1x_R$ density up ramp and a 1-mm density plateau with a ramp height of $0.002n_c$, where the n_c is the critical density. The refocusing SPM is made up of the electrons, O^{2+} and Si^{4+} ions, of which the fully ionized electron density $n_e = 200n_c$. The inner working surface is based on a paraboloid substrate, which could be expressed as $y^2 + z^2 = 2f(x_0 - x)$, where the $f = 9$ μm, $x_0 = 1050$ μm, and $\sqrt{y^2 + z^2} < 8$ μm. To prevent the penetration of the incoming laser, the longitudinal thickness of the paraboloid substrate is 2 μm. On this paraboloid substrate, the spiral stairs structure increase linearly along the azimuthal direction from 0 to $(l - 1/2)\lambda$, which could give the helical phase $e^{il\phi}$ to the incident laser, where the l is the topology charge. For simplification, the Gaussian laser was converted to the $(l,p = 1,0)$ LG mode, and the height of the stair structure would be $\lambda_L/2$, where the redshifted center wavelength $\lambda_L = 0.9$ μm. The number of macroparticle per cell is 4 in the underdense plasma region and is increased to 200 for the overdense refocusing SPM. To minimize the numerical noise in the overdense region, the fourth-order field solver was used in the simulations.

The electron motion data in the scattering process were extracted from the PIC simulations to proceed the radiation postprocessing with self-compiled codes. According to Eq. 4, we could calculate the spatial distribution of the retarded radiation field strength and the corresponding radiation spectrum that was generated by each electron. However, limited by the calculation cost, we just calculated the sample electrons from an ultrathin slice (0.01 μm) and assumed that they are in the same transverse plane. In consequence, the linear accumulation on the radiation field strength of each individual electron could be used to get the collective radiation field distribution. To obtain the accurate radiation spectrum, the prior linear interpolations on the trajectory and velocity of sample electrons are necessary before the calculation [42,43].

Figure 2 shows the properties of the accelerated electron bunches from the LWFA, including the snapshots of the spatial electron density distribution (Fig. 2A), transverse divergence angle distribution (Fig. 2B), and electron energy spectrum (Fig. 2C). Because of the critical self-injection condition, there only emerges 2 electron clusters in Fig. 2A, and the duration of each cluster $\tau_e \sim 0.1T_L$. It is obvious that the peak density of the accelerated electron bunch is about 2 magnitudes higher than the background electron density and is much higher than that of the traditional electron accelerator. When the electron bunches enter the scattering stage, it would carry the excess transverse momentum along the laser polarization direction. In the perpendicular direction with respect to the laser polarization, the electron momentum present the symmetric distribution, and the corresponding divergence angles are within 15 mrad, as shown in Fig. 2B. The energy spectrum of the accelerated electron bunches indicates the energy peak at $\gamma_e = 420$ with the energy spread near 10%.

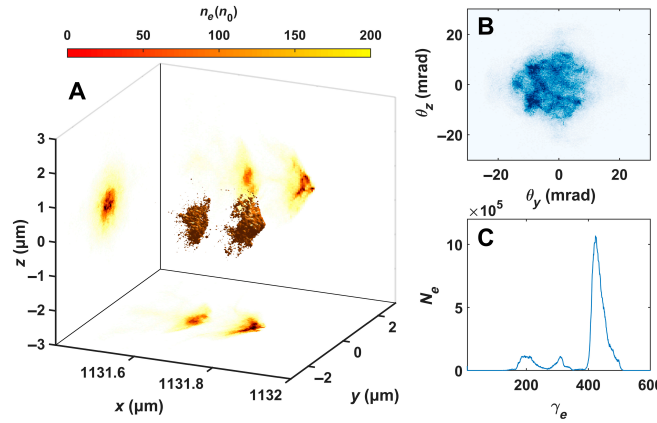

Fig. 2. The properties of accelerated electron bunches from the LWFA. The snapshots of the spatial electron density distribution and projections (A). The transverse divergence angle distribution (B) and the electron energy spectrum (C).

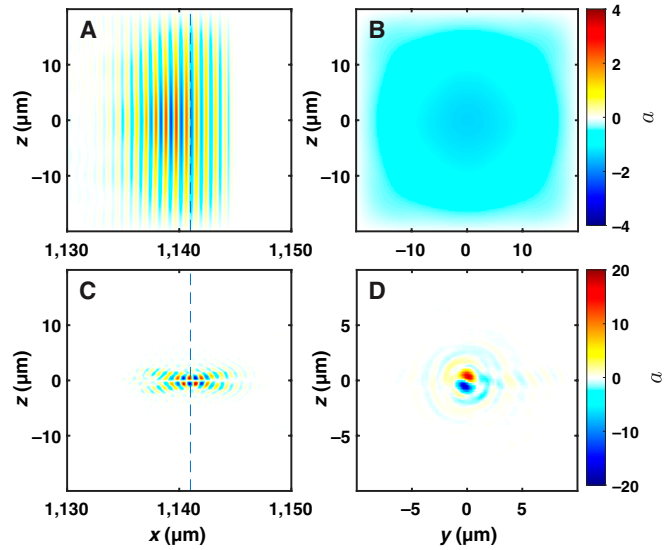

Fig. 3. The longitudinal (A and C) and transverse (B and D) distributions of the normalized laser amplitude before (A and B) and after (C and D) the refocus. The transverse distributions were taken at the positions of the corresponding dashed lines.

The transverse and longitudinal distributions of the normalized laser vector potential amplitude before (top) and after (bottom) the refocus are as shown in Fig. 3. The incident laser almost holds the Gaussian profile in transverse, and the front of laser temporal profile was steepened by the modulation of the front density gradient. By the refocusing SPM, the Gaussian laser was converted into a tightly focused LG laser with the spot radius of about 1 μm at the focal plane, as presented in Fig. 3C and D. Because of such extremely tight laser refocusing, the amplitude of the refocused LG laser was increased near 10 times to $a_0 \sim 20$, and the Thomson scattering enters the nonlinear regime. The focal plane of the refocused LG laser is exactly on the $x = 1141$ μm plane, which is the designed focal position of the paraboloid.

The electron dynamics in the scattering process could be illustrated by the evolution of transverse momentum p_y of 4 sample electrons, and the initial transverse positions are indicated in the inset, as shown in Fig. 4. Considering that the topology charge of the scattering LG laser is $l = 1$, the selection

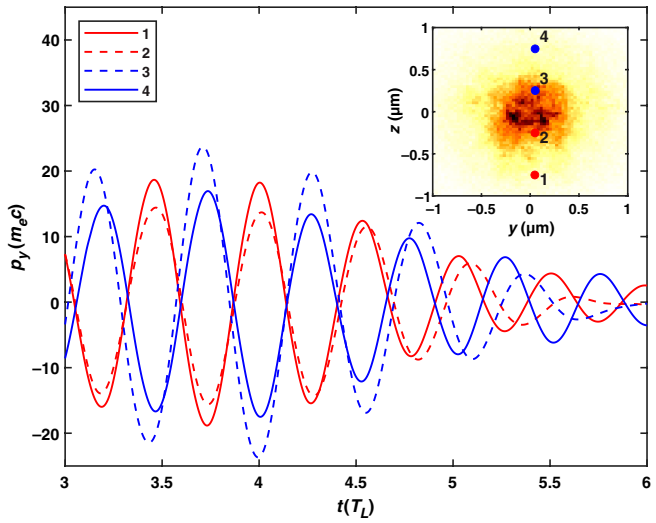

Fig. 4. The evolution of the transverse momentum p_y of 4 sample electrons in the scattering process, and the inset indicates the initial transverse positions of these 4 sample electrons.

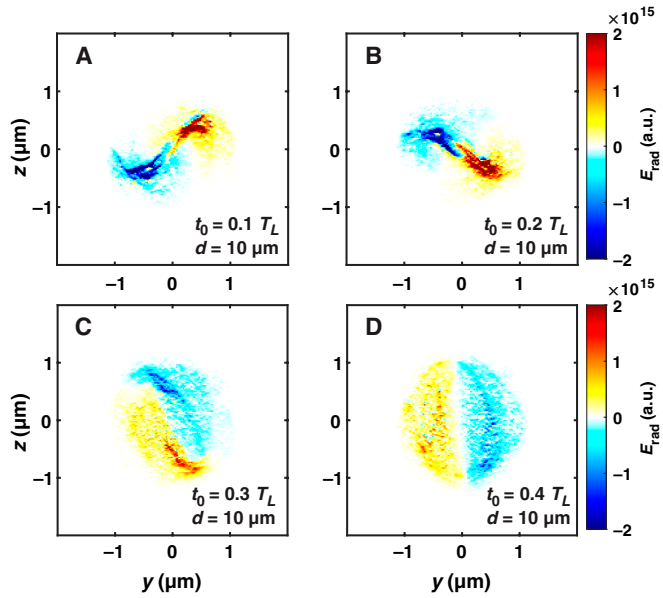

Fig. 5. The spatial distributions of the collective radiation field strength that was generated by the electron slice on the front detective plane ($d = 10$ μm) with different emission times: $t_0 = 0.1T_L$ (A), $t_0 = 0.2T_L$ (B), $t_0 = 0.3T_L$ (C), and $t_0 = 0.4T_L$ (D).

of 2 groups of sample electrons should satisfy the central symmetry to reveal the impact of the helical laser phase on the electron dynamics. The maximum amplitude of the normalized transverse momentum p_y is consistent with the a of the refocused LG laser in Fig. 3C and D. The transverse momentum p_y of the symmetric electrons would oscillate in the phase shift of π while interact with the $l = 1$ LG laser. According to Eq. 4, the collective radiation field of the electron slice was supposed to be vortical as well.

The instant snapshots of the retarded radiation field strength distributions on the co-moving detective plane ($d = 10$ μm) are presented in Fig. 5. The radiation field distributions present strange patterns, which differs from our expectation for the donut-like pattern of the scattering LG laser. The only similarity between the scattering LG laser and the radiation pattern is the identical topology charge. Moreover, the reason is that the $\hat{\boldsymbol{\beta}}$ term in Eq. 4 decides the radiation phase of the charged particles, which only delay $\pi/2$ with respect to the scattering laser phase. In consequence, the topology structure of the initial radiation field that was printed from the scattering LG laser remains unchanged, despite of the constant phase delay. In consequence, the radiation pattern was supposed to be similar with the scattering LG laser. However, this assumption was based on the premise of the linear scattering regime, in which the laser field works as the undulator, and the transverse deflection of radiation emission is too small to consider. When the scattering laser become extreme relativistic, the role of the $\boldsymbol{\beta}$ term that determines the radiation deflection comes into play, which would cause the redistribution of the radiation field.

Figure 6 shows the evolution of the radiation field on the initial emission plane and the co-moving detective plane (insets). The corresponding vector potential distributions (red arrows) of the LG scattering laser are also presented as references. The $\boldsymbol{\beta}$ in Eq. 4 decides the observation direction of the radiation peak that is to say the deflection angle of the radiation emission. Therefore, this radiation deflection would be negligible in the linear scattering regime when $a \ll 1$, and considerable radiation deflection arises when the scattering laser becomes extreme relativistic. By fixing the parameters of the scattering laser and electron bunches, the redistributed radiation field on the detective plane was determined by the observation distance d. On the initial emission plane, when $d = 0$, the radiation field distributions remain identical with the LG scattering laser. With the increase of the observation distance, the irradiating position on the detective plane would consequently deflect along the local laser vector potential (red arrows), as shown in the insets. In the backscattering configuration, the redistributed radiation field that inherit the OAM of the scattering LG laser would rotate in the angular frequency $\Omega' = 2\Omega$, where the Ω is the angular frequency of the scattering laser. In addition, the radiation pattern would continuously evolve in period. The reason for this interesting phenomenon is the variation of the distortion field that electron experiences. The radiation intensity is proportional to the $\hat{\boldsymbol{\beta}}$ term, and the local laser field that each petal experience, i.e., which continuously shapes the petal into different patterns, varies as the rotation. The collective radiation power is almost constant in one period; hence, the radiation field strength is inversely proportional to the petal area, which could be easily seen in Figs. 5 and 6. In the aspect of the angular momentum conversion, the $\vec{r} \times \vec{E}_{\mathrm{rad}}$ could be regarded as the electromagnetic moment of inertia of the radiation field, which is near constant as the evolution of the radiation pattern.

The angular distribution of the radiation intensity and the radiation spectra were calculated by the built-in Quantum electrodynamics (QED) module (Fig. 7A and B) of the PIC code and the classic electrodynamics method (Fig. 7C and D), as presented in Fig. 7. Considering the extremely relativistic intensity of the scattering LG laser, the QED module was triggered to work as the auxiliary verification, but the effect of the radiation reaction is still negligible. The total photon yield obtained from the QED module was used to estimate the quantitative spectra of the classic electrodynamics method. By comparing Fig. 7A to C, the angular distribution obtained from these 2 methods are in good agreement. The radiation divergence angles in the laser polarization and its perpendicular directions are within 25 and 10 mrad, respectively. The split and deviation of

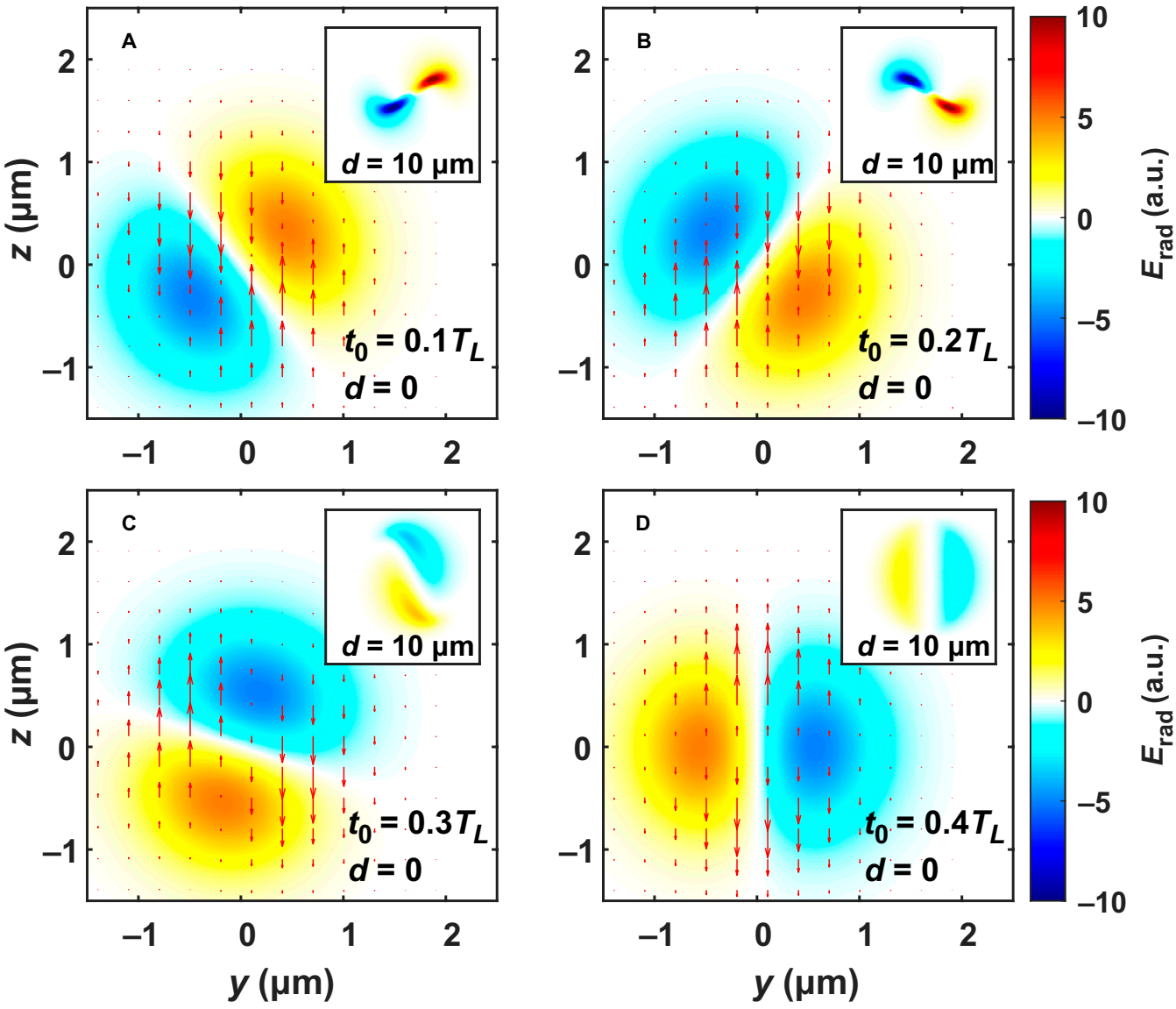

Fig. 6. The theoretic spatial distributions of the radiation field strength on the initial emission plane ($d = 0$) with different emission times: $t_0 = 0.1T_L$ (A), $t_0 = 0.2T_L$ (B), $t_0 = 0.3T_L$ (C), and $t_0 = 0.4T_L$ (D), and the corresponding redistributed radiation field distributions on the co-moving detective plane ($d = 10$ μm) are presented in the insets. The instant vector potential distributions of the LG scattering laser are shown by the red arrows.

the divergence distributions came from the excess transverse momentum that was obtained in the wake field, which could be seen in Fig. 2B. The comparison of the photon energy spectrum from the refocusing SPM scheme and the flat SPM scheme illustrated the significant increase of photon yield in the hard x-ray to gamma-ray range thanks to the refocusing SPM, as shown in Fig. 7B and D. According to the spectra obtained from the QED module, the photon yield above 100 keV is about 4.3×10^7 photons per shot, and the peak radiation brightness was estimated to be 1×10^{22} photons/s/mm^2/mrad^2/0.1% BW at 1 MeV.

Conclusions

In summary, this work investigated the gamma-ray vortex burst in the nonlinear Thomson scattering when the energetic electron bunch from the LWFA collides with the ultra-intense LG laser that was reflected from the refocusing SPM. The normal Gaussian laser drives the wake field in the underdense plasma, which could accelerate the injected electrons to a moderate energy. A refocusing SPM at the exit could convert and refocus the incident Gaussian drive laser into a tightly focused ultra-intense LG laser. As a result, the gamma-ray vortex bursts in the nonlinear Thomson scattering process. The mechanism of the twisted radiation was proved by the electron dynamics in the scattering, and the interesting radiation field distortion phenomenon due to the nonlinear effect was discovered in this process. When the deflection angle of radiation emission that was determined by the a/γ becomes considerable in the nonlinear scattering regime, the collective radiation field would be twisted by the LG laser field. However, the electromagnetic moment of inertia of the evolving radiation pattern would be nearly constant because of the angular momentum conservation. Compared with the flat SPM configuration, the refocusing SPM will boost the yield of vortical high-energy photons to 4.3×10^7 photons per shot, and the peak brightness of the twisted radiation was estimated to be 1×10^{22} photons/s/

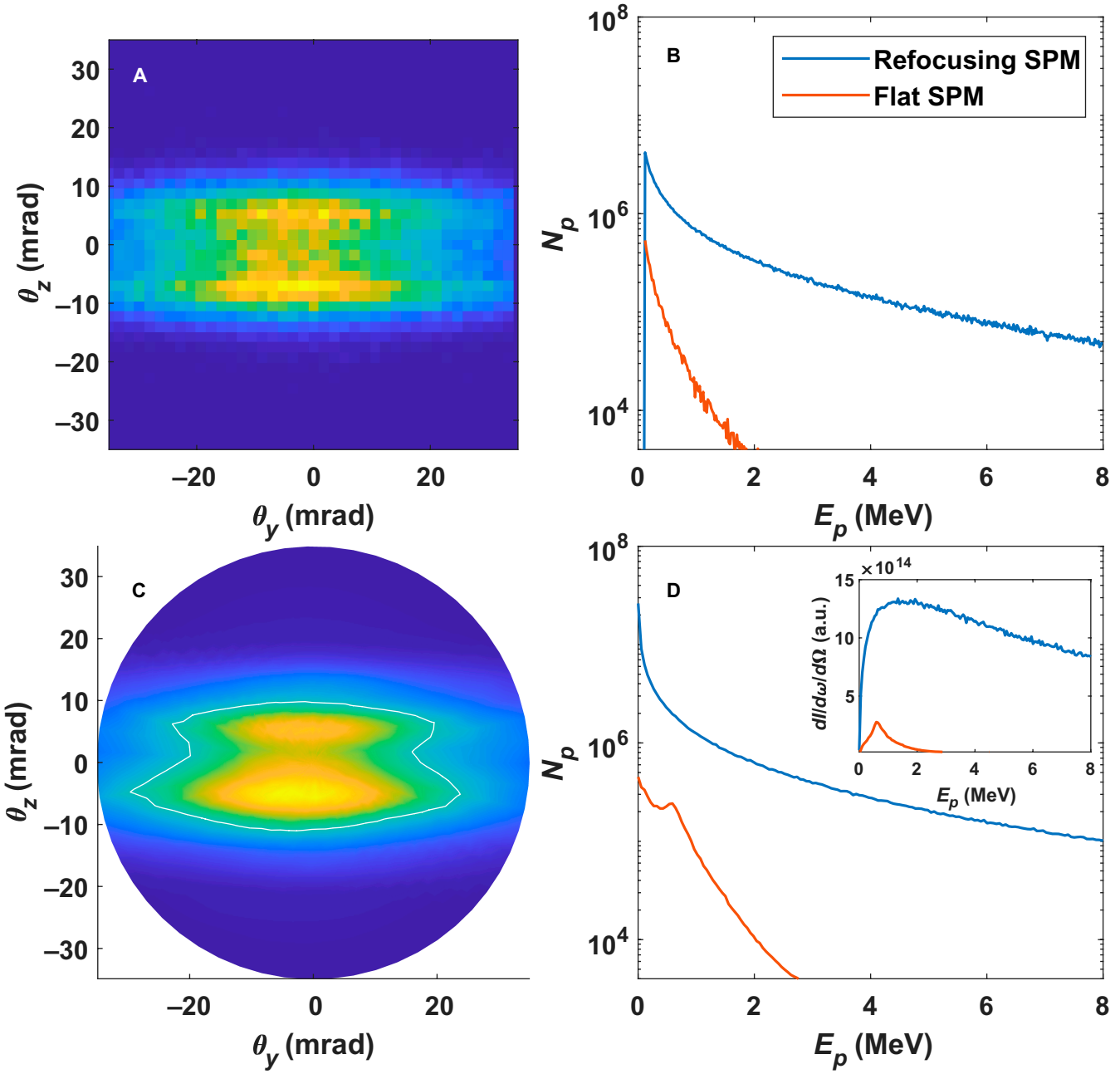

Fig. 7. The angular distribution of radiation intensity (left) and radiation spectra (right) that was obtained from the QED module (A and B) and the classic electrodynamics method (C and D). The blue and red lines in the radiation spectra (B and D) indicate the results of the refocusing SPM case and the flat SPM case, respectively.

$mm^2/mrad^2/0.1\%$ BW at 1 MeV, which might contribute to the researches on nuclei excitation, astrophysics, and angular momentum-related nuclear physics.

Acknowledgments

Funding: This work is supported by the National Key R&D Program of China (2021YFA1601700), the National Natural Science Foundation of China (12074251, 11991073, 12105174, and 11905289), the Science Challenge Project (TZ2018005), and the Strategic Priority Research Program of the CAS (XDA01020304). We thank the sponsorship from the Yangyang Development Fund. **Competing interests:** The authors declare that they have no competing interests.

References

1. Coullet P, Gil L, Rocca F. Optical vortices. *Opt Commun*. 1989;73(5):403–408.
2. Allen L, Beijersbergen MW, Spreeuw RJC, Woerdman JP. Orbital angular momentum of light and the transformation of laguerre-gaussian laser modes. *Phys Rev A*. 1992;45(11):8185–8189.
3. He H, Friese MEJ, Heckenberg NR, Rubinsztein-Dunlop H. Direct observation of transfer of angular momentum to absorptive particles from a laser beam with a phase singularity. *Phys Rev Lett*. 1995;75(5):826–829.
4. Li FS, Xu TZ, Zhang WH, Qiu XD, Lu XC, Chen LX. Optical images rotation and reflection with engineered orbital angular momentum spectrum. *Appl Phys Lett*. 2018;113(16):161109.

5. Dholakia K, Simpson NB, Padgett MJ, Allen L. Second-harmonic generation and the orbital angular momentum of light. *Phys Rev A*. 1996;54(5):R3742–R3745.
6. Fickler R, Lapkiewicz R, Plick WN, Krenn M, Schaeff C, Ramelow S, Zeilinger A. Quantum entanglement of high angular momenta. *Science*. 2012;338(6107):640–643.
7. Mair A, Vaziri A, Weihs G, Zeilinger A. Entanglement of the orbital angular momentum states of photons. *Nature*. 2001;412(6844):313–316.
8. Chattrapiban N, Rogers EA, Cofield D, Hill WT, Roy R. Generation of nondiffracting bessel beams by use of a spatial light modulator. *Opt Lett*. 2003;28(22):2183–2185.
9. Peele AG, McMahon PJ, Paterson D, Tran CQ, Mancuso AP, Nugent KA, Hayes JP, Harvey E, Lai B, McNulty I. Observation of an x-ray vortex. *Opt Lett*. 2002;27(20):1752–1754.
10. Sueda K, Miyaji G, Miyanaga N, Nakatsuka M. Laguerre-gaussian beam generated with a multilevel spiral phase plate for high intensity laser pulses. *Opt Express*. 2004;12(15):3548–3553.
11. Marrucci L, Manzo C, Paparo D. Optical spin-to-orbital angular momentum conversion in inhomogeneous anisotropic media. *Phys Rev Lett*. 2006;96(16):163905.
12. Heckenberg NR, McDuff R, Smith CP, White AG. Generation of optical phase singularities by computer-generated holograms. *Opt Lett*. 1992;17(3):221.
13. Ribič PR, Gauthier D, De Ninno G. Generation of coherent extreme-ultraviolet radiation carrying orbital angular momentum. *Phys Rev Lett*. 2014;112(20):203602.
14. Wang JW, Zepf M, Rykovanov SG. Intense attosecond pulses carrying orbital angular momentum using laser plasma interactions. *Nat Commun*. 2019;10(1):5554.
15. van Veenendaal M. Interaction between x-ray and magnetic vortices. *Phys Rev B*. 2015;92(24):245116.
16. Lin ZY, Hong MH. Femtosecond laser precision engineering: From micron, submicron, to nanoscale. *Ultrafast Sci*. 2021;2021:1–22.
17. Ivanov IP. Colliding particles carrying nonzero orbital angular momentum. *Phys Rev D*. 2011;83(9):093001.
18. van Veenendaal M, McNulty I. Prediction of strong dichroism induced by x rays carrying orbital momentum. *Phys Rev Lett*. 2007;98(15):157401.
19. Friesecke G, James RD, Jüstel D. Twisted x-rays: Incoming waveforms yielding discrete diffraction patterns for helical structures. *SIAM J Appl Math*. 2016;76(3):1191–1218.
20. Jesacher A, Fürhapter S, Bernet S, Ritsch-Marte M. Shadow effects in spiral phase contrast microscopy. *Phys Rev Lett*. 2005;94(23):233902.
21. Ye L, Rouxel JR, Asban S, Rosner B, Mukamel S. Probing molecular chirality by orbital-angular-momentum-carrying x-ray pulses. *J Chem Theory Comput*. 2019;15(7):4180–4186.
22. Stamm C, Pontius N, Kachel T, Wietstruk M, Dürr HA. Femtosecond x-ray absorption spectroscopy of spin and orbital angular momentum in photoexcited ni films during ultrafast demagnetization. *Phys Rev B*. 2010;81(10):104425.
23. Bühler R, Blandford R. The surprising crab pulsar and its nebula: A review. *Rep Prog Phys*. 2014;77(6):066901.
24. Tamburini F, Thidé B, Molina-Terriza G, Anzolin G. Twisting of light around rotating black holes. *Nat Phys*. 2011;7(3):195–197.
25. Hartemann FV, Troha AL, Baldis HA, Gupta A, Kerman AK, Landahl EC, Luhmann Jr NC, Van Meter JR. High-intensity scattering processes of relativistic electrons in vacuum and their relevance to high-energy astrophysics. *ApJS*. 2000;127(2):347–356.
26. Rubinsztein-Dunlop H, Forbes A, Berry MV, Dennis MR, Andrews DL, Mansuripur M, Denz C, Alpmann C, Banzer P, Bauer T. Roadmap on structured light. *J Opt*. 2017;19(1):013001.
27. Maurer-Grubinger C, Bernet S, Ritsch-Marte M. *Twisted photons*. Weinheim (Germany): Wiley; 2011. Chapter 8, Spiral phase contrast microscopy; p. 143–154.
28. Liu Y-Y, Salamin YI, Dou Z-K, Xu Z-F, Li J-X. Vortex γ rays from scattering laser bullets off ultrarelativistic electrons. *Opt Lett*. 2020;45(2):395–398.
29. Chen Y-Y, Li J-X, Hatsagortsyan KZ, Keitel CH. γ-ray beams with large orbital angular momentum via nonlinear Compton scattering with radiation reaction. *Phys Rev Lett*. 2018;121(7):074801.
30. Chen Y-Y, Hatsagortsyan KZ, Keitel CH. Generation of twisted γ-ray radiation by nonlinear thomson scattering of twisted light. *Matter Radiat Extrem*. 2019;4(2):024401.
31. Liu K, Yu T, Zou D, Xu X, Yin Y, Shao F. Twisted radiation from nonlinear Thomson scattering with arbitrary incident angle. *Eur Phys J D*. 2020;74(1):7.
32. Taira Y, Hayakawa T, Katoh M. Gamma-ray vortices from nonlinear inverse Thomson scattering of circularly polarized light. *Sci Rep*. 2017;7(1):5018.
33. Petrillo V, Dattoli G, Drebot I, Nguyen F. Compton scattered x-gamma rays with orbital momentum. *Phys Rev Lett*. 2016;117(12):123903.
34. Sasaki S, McNulty I. Proposal for generating brilliant x-ray beams carrying orbital angular momentum. *Phys Rev Lett*. 2008;100(12):124801.
35. Geng H-P, Chen J-H, Zhao Z-T. Scheme for generating 1 nm X-ray beams carrying orbital angular momentum at the SXFEL. *Nucl Sci Techniques*. 2020;31(9):88.
36. Wang X, Liu X, Lu X, Chen J, Long Y, Li W, Chen H, Chen X, Bai P, Li Y, et al. 13.4 fs, 0.1 Hz OPCPA front end for the 100 PW-class laser facility. *Ultrafast Science*. 2022;2022:9894358.
37. Jackson JD. *Classical electrodynamics*. 3rd ed. New York (NY): Wiley; 1998.
38. Esarey E, Ride SK, Sprangle P. Nonlinear Thomson scattering of intense laser pulses from beams and plasmas. *Phys Rev E Stat Phys Plasmas Fluids Relat Interdiscip Topics*. 1993;48(4):3003–3021.
39. Feng J, Wang J, Li Y, Zhu C, Li M, He Y, Li D, Wang W, Chen L. Intense γ ray generated by refocusing laser pulse on wakefield accelerated electrons. *Phys Plasmas*. 2017;24(9):093110.
40. Nie Z, Pai C-H, Hua J, Zhang C, Wu Y, Wan Y, Li F, Zhang J, Cheng Z, Su Q, et al. Relativistic single-cycle tunable infrared pulses generated from a tailored plasma density structure. *Nat Photon*. 2018;12(8):489–494.
41. Arber TD, Bennett K, Brady CS, Lawrence-Douglas A, Ramsay MG, Sircombe NJ, Gillies P, Evans RG, Schmitz H, Bell AR, et al. Contemporary particle-in-cell approach to laser-plasma modelling. *Plasma Phys Control Fusion*. 2015;57(11):113001.
42. Chen M, Esarey E, Geddes CGR, Schroeder CB, Plateau GR, Bulanov SS, Rykovanov S, Leemans WP. Modeling classical and quantum radiation from laser-plasma accelerators. *Phys Rev Accel Beams*. 2013;16(3):030701.
43. Thomas AGR. Algorithm for calculating spectral intensity due to charged particles in arbitrary motion. *Phys Rev Accel Beams*. 2010;13(2):020702.